Mon. Not. R. Astron. Soc. **363,** 93–106 (2005) doi:10.1111/j.1365-2966.2005.09411.x

Early afterglows in wind environments revisited

Y. C. Zou,★ X. F. Wu★ and Z. G. Dai★
Department of Astronomy, Nanjing University, Nanjing 210093, China

Accepted 2005 July 6. Received 2005 July 3; in original form 2005 February 23

ABSTRACT

When a cold shell sweeps up the ambient medium, a forward shock and a reverse shock will form. We analyse the reverse-forward shocks in a wind environment, including their dynamics and emission. An early afterglow is emitted from the shocked shell, e.g. an optical flash may emerge. The reverse shock behaves differently in two approximations: the relativistic and Newtonian cases, which depend on the parameters, e.g. the initial Lorentz factor of the ejecta. If the initial Lorentz factor is much less than $114E_{53}^{1/4}\Delta_{0,12}^{-1/4}A_{*,-1}^{-1/4}$, the early reverse shock is Newtonian. This may take place for the wider of a two-component jet, an orphan afterglow caused by a low initial Lorentz factor and so on. The synchrotron self-absorption effect is significant especially for the Newtonian reverse shock case, as the absorption frequency $\nu_{\rm a}$ is larger than the cooling frequency $\nu_{\rm c}$ and the minimum synchrotron frequency $\nu_{\rm m}$ for typical parameters. For the optical to X-ray band, the flux is nearly unchanged with time during the early period, which may be a diagnostic for the low initial Lorentz factor of the ejecta in a wind environment. We also investigate the early light curves with different wind densities and compare them with those in the interstellar medium model.

Key words: shock waves – stars: winds, outflows – gamma-rays: bursts.

1 INTRODUCTION

Long-duration gamma-ray bursts (GRBs) may originate from the collapse of massive stars (Woosley 1993; Paczyński 1998). The probable associations between GRBs and supernovae have been detected in several cases, e.g. the most confirmed GRB 980425/SN 1998bw (Galama et al. 1998; Kulkarni et al. 1998) and GRB 030329/SN 2003dh (Hjorth et al. 2003), which give a firm link to the collapsar model. The light curves of several afterglows also show the supernova component, such as GRB 970228 (Reichart 1999), 980326 (Bloom et al. 1999), 011121 (Bloom et al. 2002; Greiner et al. 2003), 021004 (Schaefer et al. 2003) and so on. Thus, the surrounding environment is wind-type. Much work concerning wind-type environment analyses has been performed (Dai & Lu 1998; Mészáros, Rees & Wijers 1998; Chevalier & Li 2000; Panaitescu & Kumar 2000), including the features of the afterglow light curves and the comparison with the interstellar medium (ISM) model.

At the beginning of the interaction between the ejected shell and the environment, an early afterglow will emerge from the reverse shock, as predicted by Mészáros & Rees (1997) and Sari & Piran (1999b). Prompt optical emission from GRB 990123 (Akerlof et al. 1999) and GRB 021211 (Fox et al. 2003; Li et al. 2003) were observed, though observations of a very early afterglow were difficult before the launch of *Swift* (Gehrels et al. 2004). The optical flash of GRB 990123 was immediately analysed (Mészáros & Rees 1999; Sari & Piran 1999a). They pointed out that the optical flashes mainly come from the contribution of the reverse shock. Then, plenty of theoretical analyses were advanced. The dynamics, numerical results of optical and radio emission, and analytical light curves, from the reverse and forward shocks in uniform environments were discussed (Sari & Piran 1995; Kobayashi 2000; Kobayashi & Sari 2000). Early afterglows in wind environments were also considered by several groups (Chevalier & Li 2000; Kobayashi & Zhang 2003; Wu et al. 2003). Panaitescu & Kumar (2004) considered the reverse-forward shock scenario and the wind bubble scenario for the two observed optical flashes from GRB 990123 and 021211. However, there has been little discussion of a Newtonian reverse shock in a wind environment. We consider this case in the following sections.

Kobayashi, Mészáros & Zhang (2004) noted the synchrotron self-absorption (SSA) effect on the early afterglow. We find that other parameters such as the thickness of the shell and the initial isotropic kinetic energy can also influence the self-absorption, even up to the optical wavelength. In this paper, we derive the complete scaling laws of the SSA frequency for all cases.

In the simulations of Zhang, Woosley & MacFadyen (2003), the initial Lorentz factor can be as low as approximately tens. For the structured jet model (Kumar & Granot 2003), it is likely that the jet has low Lorentz factors at the wings of the jet. Huang, Dai & Lu (2002) considered that a jet with an initial Lorentz factor less than 50 may cause an orphan afterglow. Rhoads (2003) also pointed out that the fireball

★E-mail: zouyc@nju.edu.cn (YCZ); xfwu@nju.edu.cn (XFW); dzg@nju.edu.cn (ZGD)

with a low initial Lorentz factor will produce a detectable afterglow, though no gamma-ray emission is detectable. There are indications that some GRBs ejecta have two components: a narrow ultrarelativistic inner core, and a wide mildly relativistic outer wing (Berger et al. 2003; Huang et al. 2004; Peng et al. 2005; Wu et al. 2005). When the mildly relativistic shell collides with the wind environment, the reverse shock is Newtonian. Kobayashi (2000) considered the Newtonian reverse shock in a uniform environment. However, no systematic analysis has come into the Newtonian reverse shock in a wind environment. In this work, we discuss the Newtonian reverse shock, which is mainly caused by a low initial Lorentz factor. In this case, the optical emission flux from the Newtonian shocked region exceeds that from the relativistic forward shocked region.

Some authors have used the early afterglow as a diagnostic tool of the parameters of gamma-ray bursts for the ISM case (Zhang, Kobayashi & Mészáros 2003a; Nakar & Piran 2004) and for the wind case (Fan, Wei & Wang 2004; Fan, Zhang & Wei 2005). Accordingly, the behaviour of early reverse-forward shocks should be completely described for the wind case. We derive the analytical scaling laws of dynamics and radiation for both relativistic and Newtonian reverse shock cases in the wind environment in Sections 2 and 3, and give the numerical results of radio to X-ray light curves in Section 4. We present some discussions in Section 5.

2 HYDRODYNAMICS

Let us consider a uniform and cold relativistic coasting shell with isotropic kinetic energy E_0, Lorentz factor $\gamma_4 = \eta + 1 \gg 1$ and width in the observer's frame Δ_0, ejected from the progenitor of the GRB. This shell sweeps up a free wind environment with number density $n_1 = Ar^{-2}$, where η is the initial ratio of E_0 to the rest mass of the ejecta (Piran, Shemi & Narayan 1993). The interaction between the shell and the wind develops a forward shock propagating into the wind and a reverse shock propagating into the shell. The two shocks separate the system into four regions: (1) the unshocked approximately stationary wind (called region 1 hereafter), (2) the shocked wind (region 2), (3) the shocked shell material (region 3) and (4) the unshocked shell material (region 4). By using the shock jump conditions (Blandford & McKee 1976, BM hereafter) and assuming the equality of pressures and velocities beside the surface of the contact discontinuity, the values of the Lorentz factor γ, the pressure p and the number density n in the shocked regions can be estimated as functions of n_1, n_4 and η, where $n_4 = E_0/(\eta 4\pi r^2 \gamma_4 \Delta_0 m_p c^2)$ is the comoving number density of region 4.

Analytical results can be obtained in both the relativistic and the Newtonian reverse shock limit. These two cases are divided by comparison between f and γ_4^2, where $f \equiv n_4/n_1$ is the ratio of the number densities between the unshocked shell and the unshocked wind (Sari & Piran 1995). As shown by Wu et al. (2003) for the wind environment case, $f = l/(\eta^2 \Delta_0)$, where $l = E_0/(4\pi A m_p c^2)$ is the Sedov length. If $f \gg \gamma_4^2$, the reverse shock is Newtonian (NRS) and if $f \ll \gamma_4^2$, the reverse shock is relativistic (RRS).

As discussed by Kobayashi & Sari (2000), even for NRS, the adiabatic index of the post-shocked fluid can be taken as a constant $\hat{\gamma} = \frac{4}{3}$, because the electrons are still relativistic. Then the shock jump conditions can read (BM; Sari & Piran 1995)

$$e_2/n_2 m_p c^2 = \gamma_2 - 1, \quad n_2/n_1 = 4\gamma_2 + 3, \tag{1}$$

$$e_3/n_3 m_p c^2 = \bar{\gamma}_3 - 1, \quad n_3/n_4 = 4\bar{\gamma}_3 + 3, \tag{2}$$

where m_p is the proton mass, e_2 and e_3 are the comoving energy densities of regions 2 and 3, respectively, and n_2 and n_3 are the corresponding comoving number densities of particles, which are assumed to consist of protons and electrons. The relative Lorentz factor between regions 3 and 4 is

$$\bar{\gamma}_3 = \gamma_3\gamma_4\left(1 - \sqrt{1 - 1/\gamma_3^2}\sqrt{1 - 1/\gamma_4^2}\right). \tag{3}$$

Assuming $\gamma_2 = \gamma_3$, and $\gamma_2, \gamma_4 \gg 1$, $\bar{\gamma}_3$ can be expressed as $\bar{\gamma}_3 \simeq (\gamma_4/\gamma_2 + \gamma_2/\gamma_4)/2$. The asymptotic solution is $\gamma_3 \simeq \frac{1}{\sqrt{2}}\gamma_4^{1/2} f^{1/4}$, $\bar{\gamma}_3 \simeq \frac{1}{\sqrt{2}}\gamma_4^{1/2} f^{-1/4}$ for RRS, while $\gamma_3 \simeq \gamma_4$ and $\bar{\gamma}_3 - 1 \simeq \frac{4}{7}\gamma_4^2 f^{-1}$ for NRS.

The time it takes the reverse shock to cross the shell in the frame of the burster is given by (Sari & Piran 1995)

$$t_\Delta = \frac{\Delta_0}{c(\beta_4 - \beta_3)}\left(1 - \frac{\gamma_4 n_4}{\gamma_3 n_3}\right). \tag{4}$$

There are two simple limits involved in the problem: NRS and RRS, in which we can obtain analytical results. The relative Lorentz factor $\bar{\gamma}_3$ is constant in the whole reverse-shock period for RRS. t_Δ can be derived as $t_\Delta = \alpha\Delta_0\gamma_4 f^{1/2}/c$ and the corresponding radius of the shell at time t_Δ is $r_\Delta \simeq ct_\Delta = \alpha\Delta_0\gamma_4 f^{1/2} \simeq \alpha\sqrt{l\Delta_0}$, where the coefficient $\alpha = \frac{1}{2}$ for RRS and $\alpha = 3/\sqrt{14}$ for NRS. We will discuss both cases separately in the following.

2.1 Relativistic reverse shock case

In the RRS case, $f \ll \gamma_4^2$ (i.e. $\eta \gg 114 E_{53}^{1/4}\Delta_{0,12}^{-1/4}A_{*,-1}^{-1/4}$), using the relation between the observer's time and the radius $t_\oplus \simeq (1+z)r/2\gamma_3^2 c$, where z is the redshift of the GRB, we obtain $T \simeq (1+z)\Delta_0/2c \simeq 16.7(1+z)\Delta_{0,12}$ s as the RRS crossing time in the observer's frame. We adopt the conventional notation $Q = Q_k \times 10^k$ in this paper except for some special explanations. Using $e_2 = e_3$, $\gamma_2 = \gamma_3$, together with the above equations, we obtain the scaling laws of the hydrodynamic variables for time $t_\oplus < T$,

$$\bar{\gamma}_3 \simeq 1.9\eta_{2.5} E_{53}^{-1/4}\Delta_{0,12}^{1/4}A_{*,-1}^{1/4} \tag{5}$$

$$\gamma_3 = \gamma_2 \simeq 81.5 E_{53}^{1/4} \Delta_{0,12}^{-1/4} A_{*,-1}^{-1/4} \tag{6}$$

$$e_3 = e_2 \simeq 1.4 \times 10^4 E_{53}^{-1/2} \Delta_{0,12}^{-3/2} A_{*,-1}^{3/2} \left(\frac{t_\oplus}{T}\right)^{-2} \text{ erg cm}^{-3} \tag{7}$$

$$N_{e,3} \simeq 2.1 \times 10^{53} E_{53} \eta_{2.5}^{-1} \frac{t_\oplus}{T} \tag{8}$$

$$N_{e,2} \simeq 3.5 \times 10^{51} E_{53}^{1/2} \Delta_{0,12}^{1/2} A_{*,-1}^{1/2} \frac{t_\oplus}{T}, \tag{9}$$

where $A_* = 3 \times 10^{35}$ cm^{-1} and $N_{e,i}$ is the number of electrons in the shocked region i. We note that γ_3 and $\bar{\gamma}_3$ do not depend on time. This is a property of wind environments, as the densities of the shell and the ambient environment have the same power-law relation with radius $r (n \propto r^{-2})$.

After the reverse shock crosses the shell ($t_\oplus > T$), the shocked shell can be roughly described by the BM solution (Kobayashi & Zhang 2003; Wu et al. 2003; Kobayashi et al. 2004),

$$\gamma_3 \propto t_\oplus^{-3/8}, \quad n_3 \propto t_\oplus^{-9/8}, \quad e_3 \propto t_\oplus^{-3/2}, \quad r \propto t_\oplus^{1/4}, \quad N_{e,3} \propto t_\oplus^{0}, \tag{10}$$

$$\gamma_2 \propto t_\oplus^{-1/4}, \quad n_2 \propto t_\oplus^{-5/4}, \quad e_2 \propto t_\oplus^{-3/2}, \quad r \propto t_\oplus^{1/2}, \quad N_{e,2} \propto t_\oplus^{1/2}. \tag{11}$$

These variables can be scaled to the initial values ($t_\oplus = T$), which are given by the expressions for the time $t_\oplus < T$.

2.2 Newtonian reverse shock case

In the NRS case, $f \gg \gamma_4^2$, the time for the reverse shock crossing the shell is $T' \simeq t_\eta \simeq 2.9 \times 10^3 (1+z) E_{53} \eta_{1.5}^{-4} A_{*,-1}^{-1}$ s in the observer's frame, if we consider the spreading of the cold shell (Piran et al. 1993). The evolution of the hydrodynamic variables before the time T' are

$$\bar{\gamma}_3 - 1 \simeq 0.57 \frac{t_\oplus}{T'} \tag{12}$$

$$\gamma_3 = \gamma_2 \simeq \gamma_4 \tag{13}$$

$$e_3 = e_2 \simeq 5.8 E_{53}^{-2} \eta_{1.5}^{6} A_{*,-1}^{3} \left(\frac{t_\oplus}{T'}\right)^{-2} \text{ erg cm}^{-3} \tag{14}$$

$$N_{e,3} = 2.1 \times 10^{54} E_{53} \eta_{1.5}^{-1} \left(\frac{t_\oplus}{T'}\right)^{1/2} \tag{15}$$

$$N_{e,2} \simeq 6.6 \times 10^{52} E_{53} \eta_{1.5}^{-2} \frac{t_\oplus}{T'}. \tag{16}$$

What should be noted is that the values for NRS are not suitable for the mildly relativistic reverse shock case. Nakar & Piran (2004) showed the difference between the approximated analytical solution and the numerical results in the case of uniform environments. And for the spreading of the shell, f decreases with radius. At the crossing time, $\bar{\gamma}_3 \simeq 1.57$ (see equation 12), which deviates from the Newtonian reverse shock approximation. More accurate values should be calculated numerically.

After the NRS crosses the shell, the Lorentz factor of the shocked shell can be assumed to be a general power-law relation $\gamma_3 \propto r^{-g}$ (Mészáros & Rees 1999; Kobayashi & Sari 2000). However, the forward shock is still relativistic, and can be described by the BM solution. The dynamic behaviour is the same as that in the RRS case. The scaling laws for the two regions are

$$\begin{aligned} &\gamma_3 \propto t_\oplus^{-g/(1+2g)}, \quad n_3 \propto t_\oplus^{-6(3+g)/7(1+2g)}, \\ &e_3 \propto t_\oplus^{-8(3+g)/7(1+2g)}, \quad r \propto t_\oplus^{1/(1+2g)}, \quad N_{e,3} \propto t_\oplus^{0}, \end{aligned} \tag{17}$$

$$\begin{aligned} &\gamma_2 \propto t_\oplus^{-1/4}, \quad n_2 \propto t_\oplus^{-5/4}, \\ &e_2 \propto t_\oplus^{-3/2}, \quad r \propto t_\oplus^{1/2}, \quad N_{e,2} \propto t_\oplus^{1/2}. \end{aligned} \tag{18}$$

3 EMISSION

We now consider the synchrotron emission from the shocked material of regions 2 and 3. The shocks accelerate the electrons into a power-law distribution: $N(\gamma_e)\,d\gamma_e = N_\gamma \gamma_e^{-p}\,d\gamma_e (\gamma_e > \gamma_m)$, where γ_m is the minimum Lorentz factor of the accelerated electrons. Assuming that constant fractions ϵ_e and ϵ_B of the internal energy go into the electrons and the magnetic field, we have $B = \sqrt{8\pi\epsilon_B e_i}$, where e_i is the internal energy density of the shocked material. Regarding the fact that the comoving internal energy of the electrons can also be written as $\epsilon_e e = \int_{\gamma_m}^{\infty} N_\gamma \gamma_e^{-p} \gamma_e m_e c^2\, d\gamma_e$ and the comoving number density $n = \int_{\gamma_m}^{\infty} N_\gamma \gamma_e^{-p}\, d\gamma_e$, one can obtain $\gamma_m = \epsilon_e(\bar{\gamma} - 1)(m_p/m_e)(p-2)/(p-1)$, where $\bar{\gamma} = \bar{\gamma}_3$ or γ_2 corresponds to the reverse or forward shock, and $N_\gamma = n(p-1)\gamma_m^{p-1}$.

The cooling Lorentz factor γ_c is defined when the electrons with γ_c approximately radiate all their kinetic energy in the dynamical time, i.e. $(\gamma_c - 1) m_e c^2 = P(\gamma_c) t_{co}$, where $P(\gamma_e) = \frac{4}{3}\sigma_T c(\gamma_e^2 - 1)(B^2/8\pi)$ (Rybicki & Lightman 1979) is the synchrotron radiation power of an electron with Lorentz factor γ_e in the magnetic field B, t_{co} is the dynamical time in the comoving frame (Sari 1998; Panaitescu & Kumar 2000). Then the cooling Lorentz factor $\gamma_c = 6\pi m_e c/(\sigma_T B^2 t_{co}) - 1$.

The synchrotron radiation is taken to be monochromatic, and the corresponding frequency of an electron with Lorentz factor γ_e is $\nu_e = \frac{3}{2}\gamma_e^2 \nu_L$, where $\nu_L = q_e B/(2\pi m_e c)$ is the Larmor frequency and q_e is the electron charge. The critical frequencies are $\nu_m = 3(1+z)^{-1}\gamma\gamma_m^2 q_e B/(2\pi m_e c)$ and $\nu_c = 3(1+z)^{-1}\gamma\gamma_c^2 q_e B/(2\pi m_e c)$, in the observer's frame, respectively, where γ is the bulk Lorentz factor of the emitted region. Before the reverse shock crosses the shell, $\nu_{c,2} = \nu_{c,3}$ is satisfied for the two regions having the same energy density e, Lorentz factor γ and the same comoving time t_{co}.

The synchrotron self-absorption effect should not be ignored, especially at low frequencies, where the emission is modified enormously for the large optical depth. Wu et al. (2003) have given the SSA coefficient and the corresponding spectral indices. Here we quote the results of Wu et al. (2003) and derive the SSA frequency for all six cases in the following.

The initial distribution of shock-accelerated electrons is

$$N(\gamma_e) = N_\gamma \gamma_e^{-p} \qquad \gamma_m < \gamma_e < \gamma_{max}. \tag{19}$$

Taking into account the synchrotron radiation energy losses, the power-law distribution of electrons is divided into two segments (Sari, Piran & Narayan 1998), i.e.

$$N(\gamma_e) = N_\gamma \begin{cases} \gamma_e^{-2} & \gamma_c < \gamma_e < \gamma_m \\ \gamma_e^{-(p+1)} & \gamma_e > \gamma_m, \end{cases} \tag{20}$$

for the fast-cooling case ($\gamma_c < \gamma_m$), and

$$N(\gamma_e) = N_\gamma \begin{cases} \gamma_e^{-p} & \gamma_m < \gamma_e < \gamma_c \\ \gamma_e^{-(p+1)} & \gamma_e > \gamma_c, \end{cases} \tag{21}$$

for the slow-cooling case ($\gamma_c > \gamma_m$).

The self-absorption coefficients in different frequency ranges are

$$k_\nu = \frac{q_e}{B} N_\gamma \begin{cases} c_1 \gamma_1^{-(p+4)} \left(\frac{\nu}{\nu_1}\right)^{-5/3} & \nu \ll \nu_1 \\ c_2 \gamma_1^{-(p+4)} \left(\frac{\nu}{\nu_1}\right)^{-(p+4)/2} & \nu_1 \ll \nu \ll \nu_2, \\ c_3 \gamma_2^{-(p+4)} \left(\frac{\nu}{\nu_2}\right)^{-5/2} e^{-\nu/\nu_2} & \nu \gg \nu_2, \end{cases} \tag{22}$$

where $c_1 = \frac{32\pi^2}{9\times 2^{1/3}\Gamma(1/3)} \frac{p+2}{p+2/3}$, $c_2 = \frac{2\sqrt{3}\pi}{9} 2^{p/2}(p+\frac{10}{3})\Gamma(\frac{3p+2}{12})\Gamma(\frac{3p+10}{12})$, $c_3 = \frac{2\sqrt{6}\pi^{3/2}}{9}(p+2)$, ν_1 and ν_2 are the typical synchrotron frequencies of electrons of Lorentz factor γ_1 and γ_2, and $\Gamma(x)$ is the Gamma function (Wu et al. 2003).

Electrons in both segments contribute to the SSA. For simplicity, the less important segment is neglected. In general, the absorption coefficient is dominated by the electrons between γ_c and γ_m, for frequencies lower than $\max(\nu_c, \nu_m)$; and dominated by the electrons with a Lorentz factor greater than $\max(\gamma_c, \gamma_m)$, for frequencies greater than $\max(\nu_c, \nu_m)$. So, the third expression in equation (22) is always unimportant and can be neglected. We can obtain analytical expressions for the SSA frequency ν_a by taking $k_\nu L = \tau_0$,

$$\nu_a = \begin{cases} \left[c_1 \frac{q_e}{B} N_\gamma \gamma_1^{-(p_1+4)} \nu_1^{5/3} \frac{L}{\tau_0}\right]^{3/5} & \nu_a \ll \nu_1 \\ \left[c_2 \frac{q_e}{B} N_\gamma \gamma_1^{-(p_1+4)} \nu_1^{(p_1+4)/2} \frac{L}{\tau_0}\right]^{2/(p_1+4)} & \nu_1 \ll \nu_a \ll \nu_2 \\ \left[c_2 \frac{q_e}{B} N_\gamma \gamma_2^{-(p_1+4)} \nu_2^{(p_2+4)/2} \frac{L}{\tau_0}\right]^{2/(p_2+4)} & \nu_a \gg \nu_2, \end{cases} \tag{23}$$

where $L = N_e/(4\pi r^2 n)$ is the comoving width of the emission region, τ_0 can be defined to be equal to 0.35 (Frail, Waxman & Kulkarni 2000), $\gamma_1 = \min(\gamma_c, \gamma_m)$, $\gamma_2 = \max(\gamma_c, \gamma_m)$, p_1 is the power-law index of the electron distribution between γ_1 and γ_2 ($p_1 = p$ for slowing cooling, $p_1 = 2$ for fast cooling) and $p_2 = p + 1$ is the index of the electron distribution with a Lorentz factor greater than γ_2.

Because the peak spectral power $P_{\nu,max} \simeq (1+z)\gamma m_e c^2 \sigma_T B/(3q_e)$ in the observer's frame is independent of γ_e, the peak observed flux density can be given by $F_{\nu,max} = N_e P_{\nu,max}/(4\pi D^2)$ at the frequency $\min(\nu_c, \nu_m)$, where D is the luminosity distance of the gamma-ray burst.

3.1 Relativistic reverse shock case

Using the above expressions, we obtain the typical frequencies and the peak flux density in the shocked shell and the shocked wind for the RRS case,

$$\nu_{m,3} \simeq 5.9 \times 10^{15} (1+z)^{-1} \bar{\epsilon}_e^2 \epsilon_{B,-1}^{1/2} E_{53}^{-1/2} \eta_{2.5}^2 A_{*,-1} \Delta_{0,12}^{-1/2} \left(\frac{t_\oplus}{T}\right)^{-1} \text{Hz}, \tag{24}$$

$$\nu_{\rm m,2} \simeq 1.0 \times 10^{19}(1+z)^{-1}\bar{\epsilon}_{\rm e}^2 \epsilon_{B,-1}^{1/2} E_{53}^{1/2} \Delta_{0,12}^{-3/2} \left(\frac{t_\oplus}{T}\right)^{-1} \ {\rm Hz}, \tag{25}$$

$$\nu_{\rm c,2} = \nu_{\rm c,3} \simeq 1.5 \times 10^{12}(1+z)^{-1}\epsilon_{B,-1}^{-3/2} E_{53}^{1/2} \Delta_{0,12}^{1/2} A_{*,-1}^{-2} \ \frac{t_\oplus}{T} \ {\rm Hz}, \tag{26}$$

$$F_{\nu,{\rm max},3} \simeq 95.3(1+z)\epsilon_{B,-1}^{1/2} E_{53}\eta_{2.5}^{-1} A_{*,-1}^{1/2} \Delta_{0,12}^{-1} D_{28}^{-2} \ {\rm Jy}, \tag{27}$$

$$F_{\nu,{\rm max},2} \simeq 1.6(1+z)\epsilon_{B,-1}^{1/2} E_{53}^{1/2} A_{*,-1} \Delta_{0,12}^{-1/2} D_{28}^{-2} \ {\rm Jy}, \tag{28}$$

where $\bar{\epsilon}_{\rm e} \equiv \epsilon_{\rm e,-0.5} \cdot 3(p-2)/(p-1)$. Note that $F_{\nu,{\rm max},3} > F_{\nu,{\rm max},2}$, i.e. region 3 dominates the emission for the early afterglow, mainly because the number of electrons in region 3 is much larger than that in region 2.

We give the scaling law of the SSA frequency in region 3,

$$\nu_{\rm a,3} \simeq \begin{cases} 1.1 \times 10^{16}(1+z)^{-1}\epsilon_{B,-1}^{6/5} E_{53}^{-1/10} \eta_{2.5}^{-3/5} A_{*,-1}^{19/10} \Delta_{0,12}^{-19/10} \left(\frac{t_\oplus}{T}\right)^{-2} \ {\rm Hz} & \nu_{\rm a} < \nu_{\rm c} < \nu_{\rm m}, \\ 2.2 \times 10^{14}(1+z)^{-1} E_{53}^{1/6} \eta_{2.5}^{-1/3} A_{*,-1}^{1/6} \Delta_{0,12}^{-5/6} \left(\frac{t_\oplus}{T}\right)^{-2/3} \ {\rm Hz} & \nu_{\rm c} < \nu_{\rm a} < \nu_{\rm m}, \\ 4.7 \times 10^{14}(1+z)^{-1}\bar{\epsilon}_{\rm e}^{2/5}\epsilon_{B,-1}^{1/10} E_{53}^{1/30} \eta_{2.5}^{2/15} A_{*,-1}^{1/3} \Delta_{0,12}^{-23/30} \left(\frac{t_\oplus}{T}\right)^{-11/15} \ {\rm Hz} & \nu_{\rm c} < \nu_{\rm m} < \nu_{\rm a}, \\ 2.2 \times 10^{14}(1+z)^{-1}\bar{\epsilon}_{\rm e}^{-1}\epsilon_{B,-1}^{1/5} E_{53}^{2/5} \eta_{2.5}^{-8/5} A_{*,-1}^{2/5} \Delta_{0,12}^{-7/5} \left(\frac{t_\oplus}{T}\right)^{-1} \ {\rm Hz} & \nu_{\rm a} < \nu_{\rm m} < \nu_{\rm c}, \\ 1.1 \times 10^{15}(1+z)^{-1}\bar{\epsilon}_{\rm e}^{6/13}\epsilon_{B,-1}^{9/26} E_{53}^{-1/26} \eta_{2.5}^{2/13} A_{*,-1}^{9/13} \Delta_{0,12}^{-25/26} \left(\frac{t_\oplus}{T}\right)^{-1} \ {\rm Hz} & \nu_{\rm m} < \nu_{\rm a} < \nu_{\rm c}, \\ 5.2 \times 10^{14}(1+z)^{-1}\bar{\epsilon}_{\rm e}^{2/5}\epsilon_{B,-1}^{1/10} E_{53}^{1/30} \eta_{2.5}^{2/15} A_{*,-1}^{1/3} \Delta_{0,12}^{-23/30} \left(\frac{t_\oplus}{T}\right)^{-11/15} \ {\rm Hz} & \nu_{\rm m} < \nu_{\rm c} < \nu_{\rm a}, \end{cases} \tag{29}$$

where and in the following expressions for $\nu_{\rm a}$, we take $p = 2.5$. If more than one of the above expressions satisfy the followed restriction, the largest $\nu_{\rm a}$ is the true value.

In region 2,

$$\nu_{\rm a,2} \simeq \begin{cases} 9.6 \times 10^{14}(1+z)^{-1}\epsilon_{B,-1}^{6/5} E_{53}^{-2/5} A_{*,-1}^{11/5} \Delta_{0,12}^{-8/5} \left(\frac{t_\oplus}{T}\right)^{-2} \ {\rm Hz} & \nu_{\rm a} < \nu_{\rm c} < \nu_{\rm m}, \\ 5.7 \times 10^{13}(1+z)^{-1} A_{*,-1}^{1/3} \Delta_{0,12}^{-2/3} \left(\frac{t_\oplus}{T}\right)^{-2/3} \ {\rm Hz} & \nu_{\rm c} < \nu_{\rm a} < \nu_{\rm m}, \\ 7.0 \times 10^{14}(1+z)^{-1}\bar{\epsilon}_{\rm e}^{2/5}\epsilon_{B,-1}^{1/10} E_{53}^{1/10} A_{*,-1}^{4/15} \Delta_{0,12}^{-5/6} \left(\frac{t_\oplus}{T}\right)^{-11/15} \ {\rm Hz} & \nu_{\rm c} < \nu_{\rm m} < \nu_{\rm a}, \\ 4.5 \times 10^{11}(1+z)^{-1}\bar{\epsilon}_{\rm e}^{-1}\epsilon_{B,-1}^{1/5} E_{53}^{-2/5} A_{*,-1}^{6/5} \Delta_{0,12}^{-3/5} \left(\frac{t_\oplus}{T}\right)^{-1} \ {\rm Hz} & \nu_{\rm a} < \nu_{\rm m} < \nu_{\rm c}, \\ 1.9 \times 10^{15}(1+z)^{-1}\bar{\epsilon}_{\rm e}^{6/13}\epsilon_{B,-1}^{9/26} E_{53}^{1/26} A_{*,-1}^{8/13} \Delta_{0,12}^{-27/26} \left(\frac{t_\oplus}{T}\right)^{-1} \ {\rm Hz} & \nu_{\rm m} < \nu_{\rm a} < \nu_{\rm c}, \\ 7.8 \times 10^{14}(1+z)^{-1}\bar{\epsilon}_{\rm e}^{2/5}\epsilon_{B,-1}^{1/10} E_{53}^{1/10} A_{*,-1}^{4/15} \Delta_{0,12}^{-5/6} \left(\frac{t_\oplus}{T}\right)^{-11/15} \ {\rm Hz} & \nu_{\rm m} < \nu_{\rm c} < \nu_{\rm a}. \end{cases} \tag{30}$$

After the reverse shock crosses the shell ($t_\oplus > T$), the behaviour of both shocked regions can be described by the BM self-similar solution. The power-law indices of emission variables with time are given in Table 1. Another frequency $\nu_{\rm cut}$ should be introduced here (Kobayashi 2000) to substitute $\nu_{\rm c}$ for no fresh electrons. $\nu_{\rm cut}$ has the same time profile as $\nu_{\rm m}$. If $\nu_{\rm m} > \nu_{\rm cut}$, $\nu_{\rm m}$ comes down to $\nu_{\rm cut}$ for the synchrotron cooling. And if $\nu_{\rm a} > \nu_{\rm cut}$, $\nu_{\rm a}$ also comes down to $\nu_{\rm cut}$ for no electrons distributed greater than the corresponding $\gamma_{\rm cut}$. These are all represented in columns labelled ⑥ (for the NRS case) and ⑧ in Table 1.

The scaling-law indices of flux densities with time are sophisticated, as they vary with time when any two of ν, $\nu_{\rm a}$, $\nu_{\rm c}$ (or $\nu_{\rm cut}$), $\nu_{\rm m}$ cross each other, where ν is the observed frequency. These indices are given in Table 2. For the case $\nu > \nu_{\rm cut}$, the flux density decreases exponentially with observed frequency ν, then we take it to be zero, which is denoted by a short horizontal line in Table 2. The numerical results will be given in Section 4.

For the typical parameters, the order of the frequencies at $t_\oplus = T$ is $\nu_{\rm m} > \nu > \nu_{\rm a} > \nu_{\rm c}$ for both regions 3 and 2, if the considered frequency is $\nu = 4.55 \times 10^{14}$ Hz. The flux density from the shocked shell and shocked environment are

$$F_{\nu,3} \simeq 5.4(1+z)^{1/2}\epsilon_{B,-1}^{-1/4} E_{53}^{5/4} \eta_{2.5}^{-1} A_{*,-1}^{-1/2} \Delta_{0,12}^{-3/4} D_{28}^{-2} \ {\rm Jy}, \tag{31}$$

$$F_{\nu,2} \simeq 0.1(1+z)^{1/2}\epsilon_{B,-1}^{-1/4} E_{53}^{3/4} \Delta_{0,12}^{-1/4} D_{28}^{-2} \ {\rm Jy}. \tag{32}$$

Table 1. The temporal indices for the evolution of ν_m, ν_c, ν_a and $F_{\nu,\max}$. The notation denotes, respectively: ① early, NRS, region 2; ② early, NRS, region 3; ③ early, RRS, region 2; ④ early, RRS, region 3; ⑤ late, NRS, region 2; ⑥ late, NRS, region 3; ⑦ late, RRS, region 2; ⑧ late, RRS, region 3. ν_c is actually ν_{cut} at columns ⑥ and ⑧.

Variable	$t < t_\Delta$ ①③④	②	$t > t_\Delta$ ⑤⑦	⑥	⑧	Notation
ν_m	-1	1	$-\frac{3}{2}$	$-\frac{15g+24}{14g+7}$	$-\frac{15}{8}$	
ν_c	1	1	$\frac{1}{2}$	$-\frac{15g+24}{14g+7}$	$-\frac{15}{8}$	
	-2	$-\frac{23}{10}$	$-\frac{8}{5}$	$-\frac{33g+36}{70g+35}$	$-\frac{3}{5}$	$\nu_a \ll \nu_c \ll \nu_m$
ν_a	$-\frac{2}{3}$	$-\frac{5}{6}$	$-\frac{2}{3}$	$-\frac{15g+24}{14g+7}$	$-\frac{15}{8}$	$\nu_c \ll \nu_a \ll \nu_m$
(Fast cooling)	$-\frac{p+3}{p+5}$	$\frac{p-6}{p+5}$	$-\frac{3p+5}{2p+10}$	$-\frac{15g+24}{14g+7}$	$-\frac{15}{8}$	$\nu_c \ll \nu_m \ll \nu_a$
	-1	$-\frac{23}{10}$	$-\frac{3}{5}$	$-\frac{33g+36}{70g+35}$	$-\frac{3}{5}$	$\nu_a \ll \nu_m \ll \nu_c$
ν_a	-1	$\frac{p-7}{p+4}$	$-\frac{3p+6}{2p+8}$	$-\frac{(15g+24)p+32g+40}{(14g+7)p+56g+28}$	$-\frac{15p+26}{8p+32}$	$\nu_m \ll \nu_a \ll \nu_c$
(Slow cooling)	$-\frac{p+3}{p+5}$	$\frac{p-6}{p+5}$	$-\frac{3p+5}{2p+10}$	$-\frac{15g+24}{14g+7}$	$-\frac{15}{8}$	$\nu_m \ll \nu_c \ll \nu_a$
$F_{\nu,\max}$	0	$-\frac{1}{2}$	$-\frac{1}{2}$	$-\frac{11g+12}{14g+7}$	$-\frac{9}{8}$	

3.2 Newtonian reverse shock case

For NRS case, before the reverse shock crosses the shell ($t_\oplus < T'$),

$$\nu_{m,3} \simeq 4.1 \times 10^{12}(1+z)^{-1}\bar{\epsilon}_e^2 \epsilon_{B,-1}^{1/2} E_{53}^{-1} \eta_{1.5}^4 A_{*,-1}^{3/2} \frac{t_\oplus}{T'} \text{ Hz} \tag{33}$$

$$\nu_{m,2} \simeq 1.3 \times 10^{16}(1+z)^{-1}\bar{\epsilon}_e^2 \epsilon_{B,-1}^{1/2} E_{53}^{-1} \eta_{1.5}^6 A_{*,-1}^{3/2} \left(\frac{t_\oplus}{T'}\right)^{-1} \text{ Hz} \tag{34}$$

$$\nu_{c,3} = \nu_{c,2} \simeq 2.7 \times 10^{13}(1+z)^{-1} \epsilon_{B,-1}^{-3/2} E_{53} \eta_{1.5}^{-2} A_{*,-1}^{-5/2} \frac{t_\oplus}{T'} \text{ Hz} \tag{35}$$

$$F_{\nu,\max,3} \simeq 7.6(1+z)\epsilon_{B,-1}^{1/2} \eta_{1.5}^3 A_{*,-1}^{3/2} D_{28}^{-2} \left(\frac{t_\oplus}{T'}\right)^{-1/2} \text{ Jy} \tag{36}$$

$$F_{\nu,\max,2} \simeq 0.2(1+z)\epsilon_{B,-1}^{1/2} \eta_{1.5}^2 A_{*,-1}^{3/2} D_{28}^{-2} \text{ Jy.} \tag{37}$$

The SSA frequency in region 3,

$$\nu_{a,3} \simeq \begin{cases} 2.2 \times 10^{12}(1+z)^{-1} \epsilon_{B,-1}^{6/5} E_{53}^{-2} \eta_{1.5}^7 A_{*,-1}^{19/5} \left(\frac{t_\oplus}{T'}\right)^{-23/10} \text{ Hz} & \nu_a < \nu_c < \nu_m \\ 7.2 \times 10^{12}(1+z)^{-1} E_{53}^{-2/3} \eta_{1.5}^3 A_{*,-1} \left(\frac{t_\oplus}{T'}\right)^{-5/6} \text{ Hz} & \nu_c < \nu_a < \nu_m \\ 7.1 \times 10^{12}(1+z)^{-1} \bar{\epsilon}_e^{2/5} \epsilon_{B,-1}^{1/10} E_{53}^{-11/15} \eta_{1.5}^{16/5} A_{*,-1}^{11/10} \left(\frac{t_\oplus}{T'}\right)^{-7/15} \text{ Hz} & \nu_c < \nu_m < \nu_a, \\ 7.3 \times 10^{12}(1+z)^{-1} \bar{\epsilon}_e^{-1} \epsilon_{B,-1}^{1/5} E_{53}^{-1} \eta_{1.5}^4 A_{*,-1}^{9/5} \left(\frac{t_\oplus}{T'}\right)^{-23/10} \text{ Hz} & \nu_a < \nu_m < \nu_c \\ 5.8 \times 10^{12}(1+z)^{-1} \bar{\epsilon}_e^{6/13} \epsilon_{B,-1}^{9/26} E_{53}^{-1} \eta_{1.5}^4 A_{*,-1}^{43/26} \left(\frac{t_\oplus}{T'}\right)^{-9/13} \text{ Hz} & \nu_m < \nu_a < \nu_c \\ 7.9 \times 10^{12}(1+z)^{-1} \bar{\epsilon}_e^{2/5} \epsilon_{B,-1}^{1/10} E_{53}^{-11/15} \eta_{1.5}^{16/5} A_{*,-1}^{11/10} \left(\frac{t_\oplus}{T'}\right)^{-7/15} \text{ Hz} & \nu_m < \nu_c < \nu_a, \end{cases} \tag{38}$$

Table 2. The temporal indices for the evolution of flux density ($F_\nu \propto t_\oplus^\alpha$). The notation is the same as in Table 1. The dashes indicate that the radiation has vanished in those cases.

Case	$t < t_\Delta$ ①③④	②	⑤⑦	$t > t_\Delta$ ⑥	⑧
$\nu < \nu_a < \nu_c < \nu_m$	3	3	2	$\frac{5g+8}{14g+7}$	$\frac{1}{2}$
$\nu_a < \nu < \nu_c < \nu_m$	$-\frac{1}{3}$	$-\frac{5}{6}$	$-\frac{2}{3}$	$-\frac{6g+4}{14g+7}$	$-\frac{1}{2}$
$\nu_a < \nu_c < \nu < \nu_m$	$\frac{1}{2}$	0	$-\frac{1}{4}$	–	–
$\nu_a < \nu_c < \nu_m < \nu$	$-\frac{p-2}{2}$	$\frac{p-1}{2}$	$-\frac{3p-2}{4}$	–	–
$\nu < \nu_c < \nu_a < \nu_m$	3	3	2	$\frac{19g+36}{14g+7}$	$\frac{21}{8}$
$\nu_c < \nu < \nu_a < \nu_m$	$\frac{5}{2}$	$\frac{5}{2}$	$\frac{7}{4}$	–	–
$\nu_c < \nu_a < \nu < \nu_m$	$\frac{1}{2}$	0	$-\frac{1}{4}$	–	–
$\nu_c < \nu_a < \nu_m < \nu$	$-\frac{p-2}{2}$	$\frac{p-1}{2}$	$-\frac{3p-2}{4}$	–	–
$\nu < \nu_c < \nu_m < \nu_a$	3	3	2	–	–
$\nu_c < \nu < \nu_a$	$\frac{5}{2}$	$\frac{5}{2}$	$\frac{7}{4}$	–	–
$\nu_c < \nu_m < \nu_a < \nu$	$-\frac{p-2}{2}$	$\frac{p-1}{2}$	$-\frac{3p-2}{4}$	–	–
$\nu < \nu_a < \nu_m < \nu_c$	2	3	1	$\frac{5g+8}{14g+7}$	$\frac{1}{2}$
$\nu_a < \nu < \nu_m < \nu_c$	$\frac{1}{3}$	$-\frac{5}{6}$	0	$-\frac{6g+4}{14g+7}$	$-\frac{1}{2}$
$\nu_a < \nu_m < \nu < \nu_c$	$-\frac{p-1}{2}$	$\frac{p-2}{2}$	$-\frac{3p-1}{4}$	$-\frac{(15g+24)\,p+7g}{28g+14}$	$-\frac{15p+3}{16}$
$\nu_a < \nu_m < \nu_c < \nu$	$-\frac{p-2}{2}$	$\frac{p-1}{2}$	$-\frac{3p-2}{4}$	–	–
$\nu < \nu_m < \nu_a < \nu_c$	2	3	1	$\frac{5g+8}{14g+7}$	$\frac{1}{2}$
$\nu_m < \nu < \nu_a < \nu_c$	$\frac{5}{2}$	$\frac{5}{2}$	$\frac{7}{4}$	$\frac{25g+40}{28g+14}$	$\frac{23}{16}$
$\nu_m < \nu_a < \nu < \nu_c$	$-\frac{p-1}{2}$	$\frac{p-2}{2}$	$-\frac{3p-1}{4}$	$-\frac{(15g+24)\,p+7g}{28g+14}$	$-\frac{15p+3}{16}$
$\nu_m < \nu_a < \nu_c < \nu$	$-\frac{p-2}{2}$	$\frac{p-1}{2}$	$-\frac{3p-2}{4}$	–	–
$\nu < \nu_m < \nu_c < \nu_a$	2	3	1	$\frac{19g+36}{14g+7}$	$\frac{21}{8}$
$\nu_m < \nu < \nu_a$	$\frac{5}{2}$	$\frac{5}{2}$	$\frac{7}{4}$	$\frac{53g+96}{28g+14}$	$\frac{57}{16}$
$\nu_m < \nu_c < \nu_a < \nu$	$-\frac{p-2}{2}$	$\frac{p-1}{2}$	$-\frac{3p-2}{4}$	–	–

and in region 2,

$$\nu_{a,2} \simeq \begin{cases} 2.8\times10^{11}(1+z)^{-1}\epsilon_{B,-1}^{6/5}E_{53}^{-2}\eta_{1.5}^{32/5}A_{*,-1}^{19/5}\left(\frac{t_\oplus}{T'}\right)^{-2}\ \mathrm{Hz} & \nu_a<\nu_c<\nu_m \\ 2.3\times10^{12}(1+z)^{-1}E_{53}^{-2/3}\eta_{1.5}^{8/3}A_{*,-1}\left(\frac{t_\oplus}{T'}\right)^{-2/3}\ \mathrm{Hz} & \nu_c<\nu_a<\nu_m \\ 1.4\times10^{13}(1+z)^{-1}\bar{\epsilon}_e^{2/5}\epsilon_{B,-1}^{1/10}E_{53}^{-11/15}\eta_{1.5}^{10/3}A_{*,-1}^{11/10}\left(\frac{t_\oplus}{T'}\right)^{-11/15}\ \mathrm{Hz} & \nu_c<\nu_m<\nu_a, \\ 1.7\times10^{10}(1+z)^{-1}\bar{\epsilon}_e^{-1}\epsilon_{B,-1}^{1/5}E_{53}^{-1}\eta_{1.5}^{12/5}A_{*,-1}^{9/5}\left(\frac{t_\oplus}{T'}\right)^{-1}\ \mathrm{Hz} & \nu_a<\nu_m<\nu_c \\ 1.3\times10^{13}(1+z)^{-1}\bar{\epsilon}_e^{6/13}\epsilon_{B,-1}^{9/26}E_{53}^{-1}\eta_{1.5}^{54/13}A_{*,-1}^{43/26}\left(\frac{t_\oplus}{T'}\right)^{-1}\ \mathrm{Hz} & \nu_m<\nu_a<\nu_c \\ 1.6\times10^{13}(1+z)^{-1}\bar{\epsilon}_e^{2/5}\epsilon_{B,-1}^{1/10}E_{53}^{-11/15}\eta_{1.5}^{10/3}A_{*,-1}^{11/10}\left(\frac{t_\oplus}{T'}\right)^{-11/15}\ \mathrm{Hz} & \nu_m<\nu_c<\nu_a. \end{cases} \tag{39}$$

After the reverse shock crosses the shell ($t_\oplus > T'$), the temporal indices of the typical frequencies and the observed flux density are also given in Tables 1 and 2.

The frequency relations at time $t_\oplus = T'$ are $\nu > \nu_c > \nu_a > \nu_m$ for region 3 and $\nu_m > \nu > \nu_c > \nu_a$ for region 2, if $\nu = 4.55 \times 10^{14}$ Hz. The corresponding optical flux densities from regions 3 and 2 are

$$F_{\nu,3} \simeq 65(1+z)^{-1/4} \bar{\epsilon}_e^{3/2} \epsilon_{B,-1}^{1/8} E_{53}^{-1/4} \eta_{1.5}^{5} A_{*,-1}^{11/8} D_{28}^{-2} \text{ mJy}, \tag{40}$$

$$F_{\nu,2} \simeq 63(1+z)^{1/2} \epsilon_{B,-1}^{-1/4} E_{53}^{1/2} \eta_{1.5} A_{*,-1}^{1/4} D_{28}^{-2} \text{ mJy}. \tag{41}$$

4 NUMERICAL RESULTS

The above analytical results can give the approximate behaviour of variables as functions of time or frequency, but they are valid only in relativistic or Newtonian limits. In the mildly relativistic case, the analytical values deviate from the actual ones significantly (Nakar & Piran 2004). For precise results, a numerical method should be engaged.

Combining equations (1)–(3), and using the assumption of equalities between the Lorentz factors and pressures beside the surface of the contact discontinuity, one can obtain solutions of γ_2, γ_3, $\bar{\gamma}_3$, e_2, n_2 and n_3 numerically. Before the reverse shock crosses the shell, the value of γ_3 should be solved from the following equation without an approximation:

$$(\gamma_3 - 1)(4\gamma_3 + 3) = \left[\gamma_3\gamma_4\left(1 - \sqrt{1 - \frac{1}{\gamma_3^2}}\sqrt{1 - \frac{1}{\gamma_4^2}}\right) - 1\right] \times \left[4\gamma_3\gamma_4\left(1 - \sqrt{1 - \frac{1}{\gamma_3^2}}\sqrt{1 - \frac{1}{\gamma_4^2}}\right) + 3\right] f, \tag{42}$$

and then the other variables can be derived directly.

We take the parameters $\eta = 300$, $E_0 = 1.0 \times 10^{52}$ erg, $A_* = 0.1$, $\Delta_0 = 5.0 \times 10^{12}$ cm, $\epsilon_e = 0.3$, $\epsilon_B = 0.1$ and $D = 1.0 \times 10^{28}$ cm, for the RRS case. For the NRS case, we set $\eta = 30$, while keeping the same other parameters as in the RRS case. Following the above analysis, we can obtain the emission from the two shocked regions, of which the optical magnitude at frequency $\nu = 4.55 \times 10^{14}$ Hz is shown in Fig. 2 (later) for the RRS case and the NRS case, respectively. The reverse shock dominates the emission at the beginning and fades after the shock crosses the shell, which is identical for both RRS and NRS. This effect may be the cause of the so-called optical flash.

After the reverse shock crosses the shell, we choose the parameter $g = 1$ for the dynamic evolution of NRS. Kobayashi & Sari (2000) discussed that g should satisfy $\frac{3}{2} < g < \frac{7}{2}$ in the ISM environment. A similar conclusion can be drawn for the dynamics of the ejecta in the wind environment. As the NRS cannot decrease the velocity of the ejected shell effectively, the shocked ejecta should be quicker than that in the RRS case, which satisfies $\gamma_3 \propto r^{-3/2}$. On the other hand, the ejecta must lag behind the forward shock, which satisfies $\gamma_2 \propto r^{-1/2}$. So the range of g should then obey $\frac{1}{2} < g < \frac{3}{2}$. What is more, the evolutions of the hydrodynamics and the emission do not depend on the value of g sensitively. The evolution of γ with the observer's time has a narrow range from $t_\oplus^{-1/4}$ to $t_\oplus^{-3/7}$ corresponding to the range of g.

Figs 1–3 show the light curves at radio (8.46 GHz), optical band (4.55×10^{14} Hz) and X-ray (1.0×10^{18} Hz) wavelengths, respectively. The upper panel denotes the RRS case and the lower panel denotes the NRS case. At low frequencies, ν_a is always greater than the observed frequency, so the emission at these frequencies is affected by the synchrotron self-absorption enormously, and can be estimated as thermal emission at this band (Chevalier & Li 2000). The radio flux density increases with time before and shortly after the crossing time, as shown in Fig. 1, which comes from the increasing number of accelerated electrons. The flux will be intense enough to be detected if the distance is not so large, as the flux is inversely proportional to the square of the luminosity distance.

The numerical results are consistent with the analytical ones. For the typical parameters and $\nu = 4.55 \times 10^{14}$ Hz as the observed frequencies, at the crossing time, the orders of the typical frequencies are $\nu_{c,3} < \nu_{a,3} < \nu < \nu_{m,3}$ for RRS case, $\nu_{c,3} < \nu_{m,3} < \nu_{a,3} < \nu$ for NRS case, and $\nu_{c,2} < \nu_{a,2} < \nu < \nu_{m,2}$ for both cases. From Table 2, we find that the corresponding temporal indices are $\frac{1}{2}$, $-\frac{1}{4}$ and $\frac{1}{2}$ for the time before the reverse shock crosses the ejected shell, where $p = 2.5$. In Fig. 2, the slopes can be seen from the four dashed lines before the break point, which is the crossing time. The value of the flux density from region 3 at time $t = T'$ is, however, not consistent with the value (55 mJy) given by equation (40), which is ∼3.5 mJy in the figure, as the reverse shock is mildly relativistic. The curves do not accord well with the approximated analytical slopes either.[1]

For the optical band, the reverse shock dominates the emission at the beginning, and decays quickly after the crossing time, as there are no fresh shocked electrons to produce the emission. This is the same for both RRS and NRS cases, as seen in Fig. 2. However, the X-ray afterglow is always dominated by the forward shock, especially for the NRS case, as the reverse shock is not strong enough, and cannot accelerate the electrons to a high stochastic Lorentz factor to emit numerous X-ray band photons. Fig. 3 shows the emission in the X-ray band for both RRS and NRS cases. From these three figures, we can see that the main emission is approximately in the optical band.

[1] The reverse-forward shock is assumed to begin at the coasting period of the fireball, which is the initial time for the early afterglow. However, the coasting radius is not zero, though it can be neglected at late times, which has been adopted in the scaling-law analyses. Therefore, at early times, the curve in Fig. 2 for RRS case is not straight. As the curve for NRS in the figure begins at 10 s, the influence of the non-zero initial radius can be neglected now.

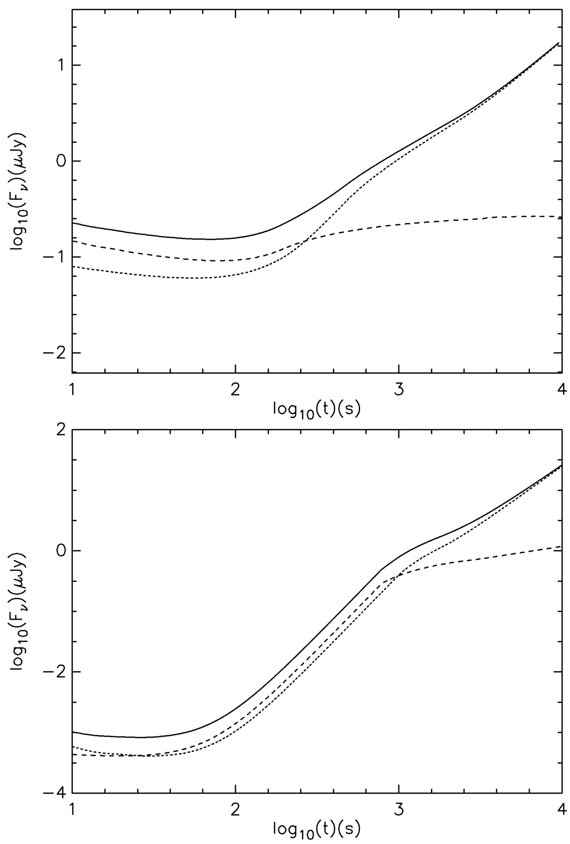

Figure 1. Flux density at $\nu = 8.46$ GHz as a function of time. Parameters are $\eta = 300$, $E_0 = 1.0 \times 10^{52}$ erg, $A_* = 0.1$, $\Delta_0 = 5.0 \times 10^{12}$ cm, $\epsilon_e = 0.3$, $\epsilon_B = 0.1$ and $p = 2.5$ for the upper panel (RRS case). Only $\eta = 30$ is different for the lower panel (NRS case). The long- and short-dashed lines represent the emission from regions 3 and 2, respectively, and the solid line is the total flux density from both regions.

As can be seen in equation (40), the flux density depends on η very sensitively. We plot the magnitude as a function of time for different η values in Fig. 4. Taking into account the lower panel in Fig. 2 and the first two in this figure, we can find that, with other parameters unchanged, the larger η, the larger the flux density, as the flux density is proportional to $\sim\eta^{8.5}$ if $p = 2.5$. When $\eta = 50$, shown in the lowest panel in Fig. 4, the reverse shock becomes mildly relativistic. In the relativistic reverse shock case, it is approximately inversely proportional to η. The flux density descends with increasing η. Another phenomenon is that, with increasing η, the time for the emission from region 2 to overtake that from region 3 postpones, and then region 3 almost dominates the emission during the whole early period. Because the number of electrons in region 3 is much larger than that in region 2, the emission is dominated by region 3, when the reverse shock is powerful enough to accelerate the electrons to emit enough optical band synchrotron photons. Thirdly, no distinct ascending of the optical light curves appears before the crossing time for the NRS case. On the contrary, the light curves will descend at the beginning if the emission is dominated by the region 3.

We plot the spectrum at the crossing time for the reverse shock and the forward shock, respectively, in Fig. 5. The spectrum is a typical synchrotron spectrum for the electron energy distribution with index $p = 2.5$. The breaks are smoothened by the equal-time arrival effect (Sari 1998). Both curves have three typical frequencies ν_a, ν_c and ν_m. The time behaviour of the frequencies before and after the crossing time is illustrated in this figure. Before the crossing time, $\nu_{m,3} \propto t^{-1/2}$, which is different from the analytical result for NRS case $\nu_{m,3} \propto t^1$ (listed in Table 1). This comes from the fact that the term $\bar{\gamma}_3 - 1$ cannot be taken to be much less than 1, especially for a shallow Newtonian reverse shock. Consequently, $\nu_{a,3}$ becomes approximately $\propto t^{-1/2}$, not $\propto t^{-(p+3)/(p+5)}$ in Table 1. For these parameters, $\nu_{m,3}$ is occasionally equal to $\nu_{c,3}$ at the crossing time. After the crossing time, as no fresh electrons are supplied, electrons with a stochastic Lorentz factor greater than γ_c disappear. The maximum electron Lorentz factor γ_{cut} varies with time like γ_m (Kobayashi 2000). The corresponding ν_{cut} does so. As one can see, the maximum typical frequency in region 3 is ν_a, so the synchrotron self-absorption effect is important for the reverse shock in the NRS case.

The wind parameter A is important for the reverse-forward shock. How do the light curves vary if the wind density varies? We give a set of light curves of the early afterglow with different A in Fig. 6. The parameter A is taken from 3×10^{32} to 3×10^{35} cm^{-1} ($A_* = 1$). With increasing A, the reverse shock converts from being Newtonian to relativistic. For the extreme NRS case, the emission is dominated by the forward shock (the lower light curves in Fig. 6). This makes the light curves (summation of regions 2 and 3) have no break at the crossing time. However, with increasing A, the early emission is gradually dominated by the reverse shock, so the breaks (in the upper light curves) appear

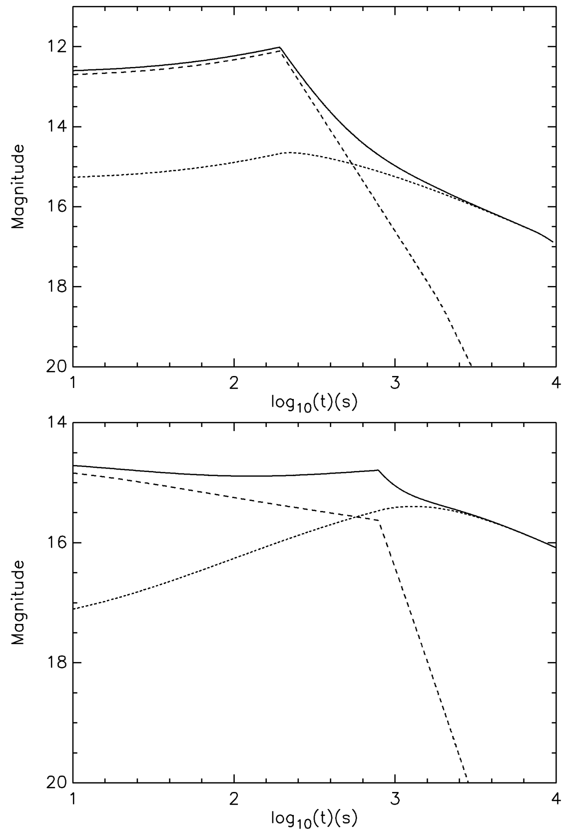

Figure 2. The optical magnitude as a function of time. Parameters are the same as in Fig. 1.

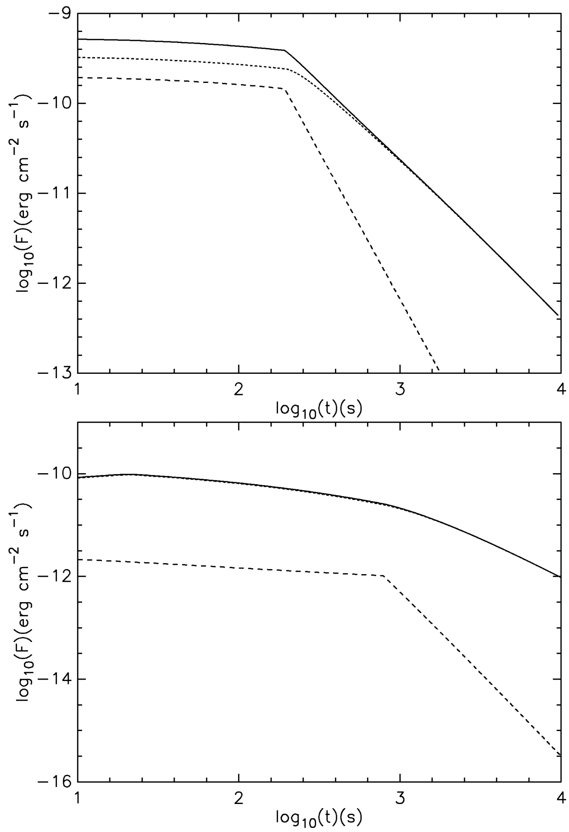

Figure 3. 2–10 keV flux as a function of time. Parameters are the same as in Fig. 1.

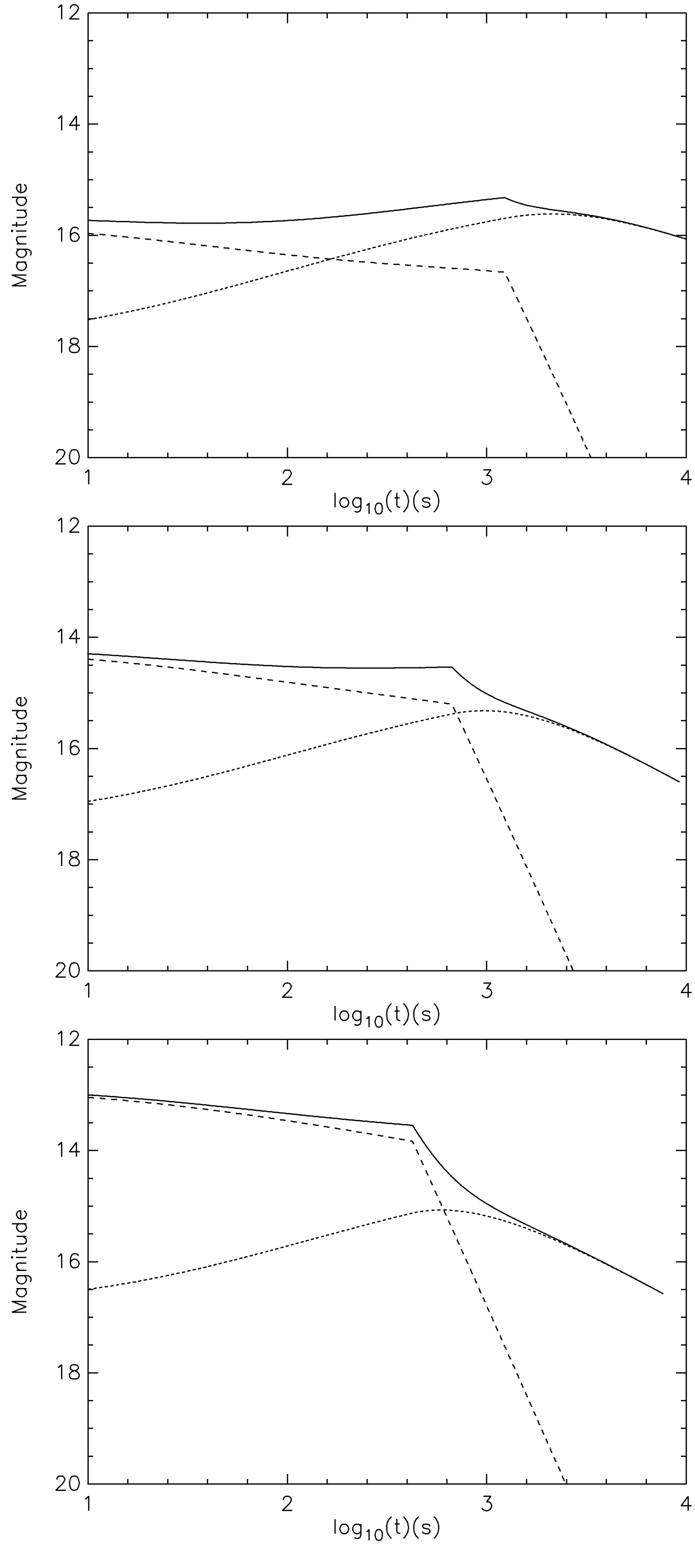

Figure 4. The magnitude as a function of time at 4.55×10^{14} Hz. Parameters are the same as in Fig. 1 except for η. η is 25, 35 and 50 from top to bottom.

at the crossing time. Another phenomenon is that, as A decreases, the crossing time becomes longer, which is mainly due to the spreading of the ejected shell. With the approximation by ignoring the spreading effect, the analytical crossing time for RRS is a constant $(1 + z)\Delta_0/2c$. In Fig. 6, we can see that the crossing time converges to $(1 + z)\Delta_0/2c = 167[(1 + z)/2]\Delta_{0,5\times10^{12}}$ s with increasing A.

The ISM environment case has been investigated extensively (Sari & Piran 1995; Mészáros & Rees 1997; Kobayashi 2000; Kobayashi & Sari 2000; Zhang et al. 2003a). Here we calculate the light curves of the reverse-forward shock for the ISM density $n_1 = 1$ cm^{-3} and

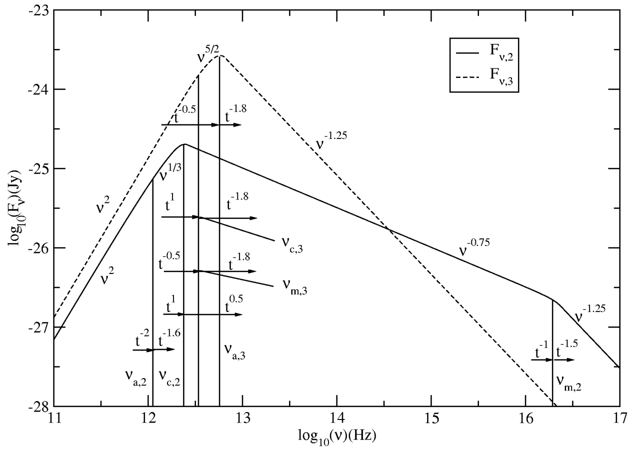

Figure 5. Flux density in region 2 (solid line) and in region 3 (dashed line) as a function of the observed frequency, at the crossing time. Parameters are the same as in Fig. 1 with $\eta = 30$. The arrows on the left of the vertical line denote the time behaviour of the corresponding typical frequencies before the crossing time and the arrows on the right denote the time behaviour after the crossing time.

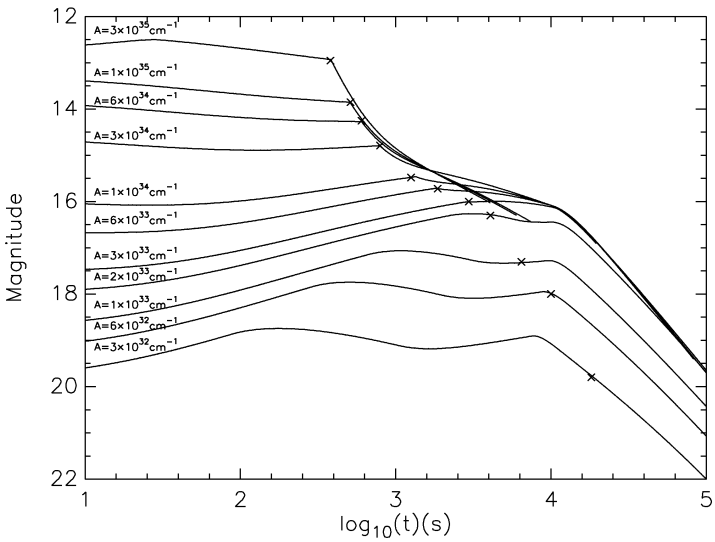

Figure 6. Light curves in the optical band (4.55×10^{14} Hz) for different values of the wind parameter A. Parameters are the same as in Fig. 1 except A, and $\eta = 30$. The crosses ($\times$) indicate the crossing time of the reverse shock.

with the other parameters being the same as the typical values in the wind environment (see Fig. 7). For these parameters, the flux densities both for the RRS case (upper panel) and for the NRS case (lower panel) increase during the early period, which are different from the wind environment case. We can see in Fig. 2 that the light curves almost stay unchanged for early times in the optical band. This may be caused by decreasing the number density of the wind. Therefore, whether or not there exists a rapid increase of the early optical afterglow may be used to distinguish between the ISM and wind environments.

5 CONCLUSIONS AND DISCUSSION

We have investigated the whole evolution of the dynamics and emission of the reverse-forward shock in a wind environment, by considering both the RRS and NRS cases. The temporal indices of the physical quantities are given in Tables 1 and 2, which cover all interrelations of the typical frequencies ν_a, ν_m, ν_c and the observed frequency ν. The flux densities of the emission at radio, optical and X-ray bands as functions of time are shown in Figs 1–3 by numerical calculations.

For the ISM model, there exists a transition radius R_N [satisfying $f(R_N) = \gamma_4^2$] for a thick shell (Sari & Piran 1995), where the reverse shock becomes relativistic. An enormous difference between the wind model and the ISM model is that the Lorentz factor of the shocked regions before the crossing time is constant with time for the wind model in the RRS case. As the transition should satisfy $f/\gamma_4^2 = 1$, the density ratio of f is constant for the wind environment, and thus no transition exists. Therefore, the relative Lorentz factor of the reverse shock $\bar{\gamma}_3$ is also independent of time. Taking into account these properties, we find that the temporal indices are relatively reliable, even

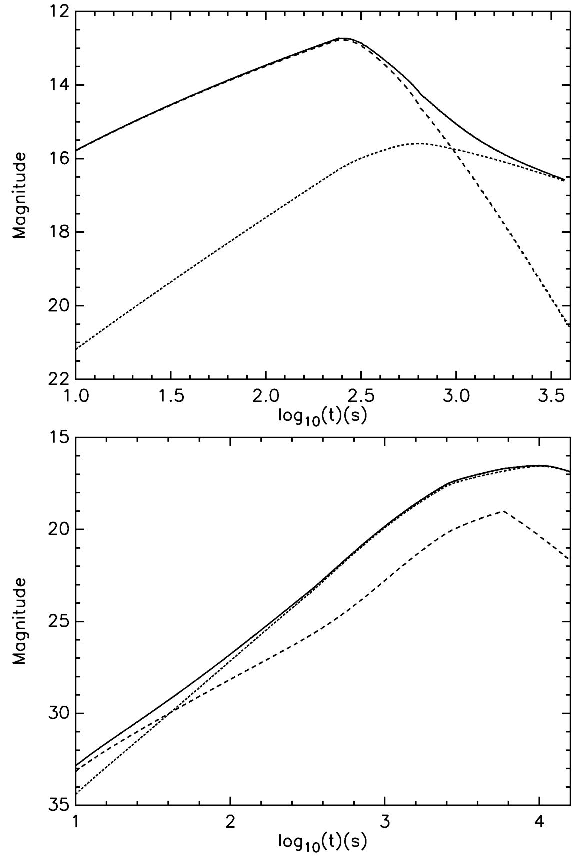

Figure 7. The magnitude at 4.55×10^{14} Hz as a function of time in the ISM environment. $n_1 = 1\ \mathrm{cm}^{-3}$ is the number density of ISM material. $\eta = 300$ for the upper panel is the RRS case, and $\eta = 30$ for the lower panel is the NRS case. Other parameters are the same as in Fig. 1.

if the estimates of the Lorentz factors $\bar{\gamma}_3$, γ_2 and γ_3 deviate from the actual values, which are caused by the Newtonian and relativistic approximations.

An optical flash emitted from the shocked shell appears for the typical parameters, but perhaps no darkening can be observed at early times. A rapid decay occurs after the reverse shock crosses the shell, and then the emission is dominated by the shocked environment material. A radio flare lasts for a longer time. It increases continuously even shortly after the crossing time. The X-ray band emission is always dominated by region 2. In the optical and X-ray bands, the flux is nearly unchanged at early times especially for the NRS case, which may be used to diagnose the NRS in a wind environment. For the reverse shock, the synchrotron self-absorption cannot be neglected, as it may exceed the other two frequencies ν_c and ν_m as the number density increases.

There is also a possibility that no prompt optical emission is detected. It may be caused by a low initial energy, a low environmental density or strong absorption and so on. These will decrease the flux density of the early afterglow to go beyond the limits of the detector. In the era of *Swift*, many early optical and X-ray afterglows will be detected by UVOT and XRT, such as GRB 050525A (Klotz et al. 2005; Shao & Dai 2005), and then the parameters may be determined by early afterglow data more precisely.

ACKNOWLEDGMENTS

We would like to thank the anonymous referee for valuable suggestions. YCZ thanks T. Yan, H. L. Dai, Y. Z. Fan and Y. F. Huang for helpful discussions. This work was supported by the National Natural Science Foundation of China (grants 10233010 and 10221001) and the Ministry of Science and Technology of China (NKBRSF G19990754).

REFERENCES

Akerlof C. et al., 1999, Nat, 398, 400
Berger E. et al., 2003, Nat, 426, 154
Blandford R. D., McKee C. F., 1976, Phys. Fluid, 19, 1130 (BM)
Bloom J. S. et al., 1999, Nat, 401, 453
Bloom J. S. et al., 2002, ApJ, 572, L45
Chevalier R. A., Li Z. Y., 2000, ApJ, 536, 195

Dai Z. G., Lu T., 1998, MNRAS, 298, 87
Fan Y. Z., Wei D. M., Wang C. F., 2004, A&A, 424, 477
Fan Y. Z., Zhang B., Wei D. M., 2005, ApJ, 628, 298
Fox D. W. et al., 2003, ApJ, 586, L5
Frail D. A., Waxman E., Kulkarni S. R., 2000, ApJ, 537, 191
Galama T. J. et al., 1998, Nat, 395, 670
Gehrels N. et al., 2004, ApJ, 611, 1005
Greiner J. et al., 2003, ApJ, 599, 1223
Hjorth J. et al., 2003, Nat, 423, 847
Huang Y. F., Dai Z. G., Lu T., 2002, MNRAS, 332, 735
Huang Y. F., Wu X. F., Dai Z. G., Ma H. T., Lu T., 2004, ApJ, 605, 300
Klotz A. et al., 2005, A&A, submitted (astro-ph/0506259)
Kobayashi S., 2000, ApJ, 545, 807
Kobayashi S., Sari R., 2000, ApJ, 542, 819
Kobayashi S., Zhang B., 2003, ApJ, 597, 455
Kobayashi S., Mészáros P., Zhang B., 2004, ApJ, 601, L13
Kulkarni S. R. et al., 1998, Nat, 395, 663
Kumar P., Granot J., 2003, ApJ, 591, 1075
Li W. D., Filippenko A. V., Chornock R., Jha S., 2003, ApJ, 586, L9
Mészáros P., Rees M. J., 1997, ApJ, 476, 232
Mészáros P., Rees M. J., 1999, MNRAS, 306, L39
Mészáros P., Rees M. J., Wijers R. A. M., 1998, ApJ, 499, 301
Nakar E., Piran T., 2004, MNRAS, 353, 647
Paczyński B., 1998, ApJ, 494, L45
Panaitescu A., Kumar K., 2000, ApJ, 543, 66
Panaitescu A., Kumar K., 2004, MNRAS, 353, 511
Peng F., Konigl A., Granot J., 2005, ApJ, 626, 966
Piran T., Shemi A., Narayan R., 1993, MNRAS, 263, 861
Reichart D. E., 1999, ApJ, 521, L111
Rhoads J. E., 2003, ApJ, 591, 1097
Rybicki G. B., Lightman A. P., 1979, Radiative Processes in Astrophysics. Wiley, New York
Sari R., 1998, ApJ, 494, L49
Sari R., Piran T., 1995, ApJ, 455, L143
Sari R., Piran T., 1999a, ApJ, 517, L109
Sari R., Piran T., 1999b, ApJ, 520, 641
Sari R., Piran T., Narayan R., 1998, ApJ, 497, L17
Schaefer B. E. et al., 2003, ApJ, 588, 387
Shao L., Dai Z. G., 2005, ApJ, in press (astro-ph/0506139)
Wu X. F., Dai Z. G., Huang Y. F., Lu T., 2003, MNRAS, 342, 1131
Wu X. F., Dai Z. G., Huang Y. F., Lu T., 2005, MNRAS, 357, 1197
Woosley S. E., 1993, ApJ, 405, 273
Zhang B., Kobayashi S., Mészáros P., 2003a, ApJ, 595, 950
Zhang W. Q., Woosley S. E., MacFadyen A. I., 2003b, ApJ, 586, 356

This paper has been typeset from a TEX/LATEX file prepared by the author.